XI International Conference on Computational Plasticity. Fundamentals and Applications
COMPLAS XI
E. Oñate, D.R.J. Owen, D. Peric and B. Suárez (Eds)

TOWARDS THE EFFECTIVE BEHAVIOUR OF POLYCRYSTALLINE MICROSTRUCTURES AT FINITE STRAINS

EVA LEHMANN[*†], STEFAN LOEHNERT[*♯] AND PETER WRIGGERS[*◇]

[*]Institute of Continuum Mechanics
Leibniz Universität Hannover
Appelstraße 11, 30167 Hannover, Germany

[†] e-mail: lehmann@ikm.uni-hannover.de,
web page: http://www.ikm.uni-hannover.de/

[♯] e-mail: loehnert@ikm.uni-hannover.de
[◇] e-mail: wriggers@ikm.uni-hannover.de

Key words: Finite Crystal Plasticity, Sheet Bulk Metal Forming, Homogenisation

Summary. It is well known that metals behave anisotropically on their microstructure due to their crystalline nature. FE-simulations in the metal forming field however sometimes lack the right macroscopic anisotropies as their type can be unspecific.

In order to find a suitable effective elastoplastic material model, a finite crystal plasticity model is used to model the behaviour of polycrystalline materials in representative volume elements (RVEs) representing the microstructure, taking into account the plastic anisotropy due to dislocations occurring within considered slip systems. A multiplicative decomposition of the deformation gradient into elastic and plastic parts is performed, as well as the split of the elastic free energy into volumetric and deviatoric parts resulting in a compact expression of the resolved SCHMID stress depending on the slip system vectors. In order to preserve the plastic incompressibility condition, the elastic deformation gradient is updated via an exponential map scheme. To further circumvent singularities stemming from the linear dependency of the slip system vectors, a viscoplastic power-law is introduced providing the evolution of the plastic slips and slip resistances.

The model is validated with experimental microstructural data under deformation. Through homogenisation and optimisation techniques, effective stress-strain curves are determined and can be compared to results from real manufacturing and fabrication processes leading to an effective elastoplastic material model which is suitable for metal forming processes at finite strains.

1 INTRODUCTION

Phenomenological macroscopic observations of metals do not acknowledge actual heterogeneities in the microstructure at once. For some time, the mechanics of heterogeneous and polycrystalline materials have been limited to the formulation of simplified models taking into account some aspects of the microstructural characteristics. However, the proceeding increase of computational capabilites enables a more elaborated approach towards the development of a suitable material model for specific requirements and numerical simulations in the forming field. At the same time, modeling the microstructure is already a complex task as certain microstructural properties have to be considered. On the microscopic level of metals, anisotropies have to be taken into account stemming from dislocations occurring on the atomic lattice within considered slip systems. Such mechanisms are macroscopically observed as plastic anisotropic yielding.

In order to take into account the microstructural complexity on the one hand and aiming at the ability to compute real manufacturing and forming processes on the other hand, a macroscopic effective material model which sufficiently represents the microstructure has to be developed. Due to the various different boundary conditions the material can be constrained to during fabrication stages, it has to be validated for these applications. A huge challenge appears in the attempt to fulfil the requirements of both sheet and bulk metal forming processes. In doing so, the model approach has naturally to be performed in a three-dimensional way, as the structure can certainly be constrained to any geometrical limit or constitution. However, the dislocation movement on the microstructure evolves in three required directions.

2 CONSTITUTIVE FRAMEWORK: MULTIPLICATIVE MULTISURFACE ELASTOPLASTICITY

The deformation gradient $\boldsymbol{F} = \frac{\partial \boldsymbol{x}}{\partial \boldsymbol{X}}$ with Jacobian $\mathrm{J} = \det \boldsymbol{F} > 0$ maps tangent vectors of material lines in the reference configuration $\mathcal{B} \in \mathbb{R}^3$ onto tangent vectors of deformed lines in the current configuration $\mathcal{B}_\mathrm{t} \in \mathbb{R}^3$ and is decomposed into an elastic and a plastic part. The elastic part $\boldsymbol{F}^e$ contributes to stretching and rigid body rotation of the crystal lattice, the plastic part $\boldsymbol{F}^p$ characterises plastic flow caused by dislocations on defined slip systems

$$\boldsymbol{F} = \boldsymbol{F}^e \boldsymbol{F}^p. \tag{1}$$

The multiplicative split assumes a local unstressed intermediate configuration defined by the plastic deformation gradient, see Fig. 1, which can be determined through an evolution assumption and whose initial condition is assumed to be $\boldsymbol{F}^p_0 = \boldsymbol{1}$.

Further, a volumetric-deviatoric split of the deformation gradient and its constituents is performed

$$\boldsymbol{F}_\mathrm{iso} = \mathrm{J}^{-1/3} \boldsymbol{F}, \quad \boldsymbol{F}^e_\mathrm{iso} = \mathrm{J}^{e\,-1/3} \boldsymbol{F}^e, \quad \boldsymbol{F}^p_\mathrm{iso} = \mathrm{J}^{p\,-1/3} \boldsymbol{F}^p, \tag{2}$$

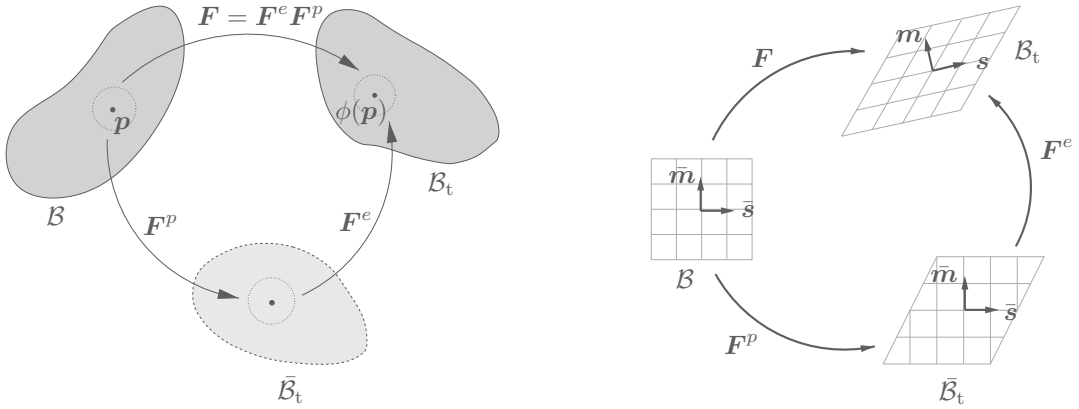

(a) Continuum mechanical framework (b) Crystallographic conception

Figure 1: Multiplicative elasto-plastic decomposition of the deformation gradient $\boldsymbol{F}$

with $\mathrm{J} = \mathrm{J}^e$ due to fulfilling the requirement of present plastic incompressibility expressed through $\mathrm{J}^p = 1$.

2.1 Thermodynamical considerations

The deformation power per unit undeformed volume can be written as

$$\boldsymbol{P} : \dot{\boldsymbol{F}} = \bar{\boldsymbol{P}} : \dot{\boldsymbol{F}}^e + \bar{\boldsymbol{\Sigma}} : \bar{\boldsymbol{L}}^p, \tag{3}$$

where $\bar{\boldsymbol{P}} = \boldsymbol{P}\boldsymbol{F}^{p\,T}$ is the 1st PIOLA-KIRCHHOFF stress tensor relative to the intermediate configuration $\bar{\mathcal{B}}_\mathrm{t}$ and $\bar{\boldsymbol{\Sigma}} = \boldsymbol{F}^{e\,T}\boldsymbol{P}\boldsymbol{F}^{p\,T} = \boldsymbol{F}^{e\,T}\boldsymbol{\tau}\boldsymbol{F}^{e\,-T}$ a stress measure conjugate to the plastic velocity gradient $\bar{\boldsymbol{L}}^p = \dot{\boldsymbol{F}}^p\boldsymbol{F}^{p\,-1}$ on $\bar{\mathcal{B}}_\mathrm{t}$, $\boldsymbol{\tau}$ being the KIRCHHOFF stress tensor on $\mathcal{B}_\mathrm{t}$. Further, it is

$$\bar{\boldsymbol{P}} = \boldsymbol{F}^e\bar{\boldsymbol{S}}, \quad \bar{\boldsymbol{S}} = \bar{\boldsymbol{C}}^{e\,-1}\bar{\boldsymbol{\Sigma}}, \quad \bar{\boldsymbol{C}}^e = \boldsymbol{F}^{e\,T}\boldsymbol{F}^e, \tag{4}$$

where $\bar{\boldsymbol{S}}$ is the 2nd PIOLA-KIRCHHOFF stress tensor relative to the intermediate configuration $\bar{\mathcal{B}}_\mathrm{t}$ which is symmetric, $\bar{\boldsymbol{C}}^e$ is further the elastic right CAUCHY-GREEN tensor on $\bar{\mathcal{B}}_\mathrm{t}$.

The evolution of the plastic deformation gradient $\boldsymbol{F}^p$ is defined by the plastic flow equation, resulting from the plastic rate of deformation $\bar{\boldsymbol{L}}^p$. In the presence of n_syst systems undergoing plastic slip, represented by the plastic shear rates $\dot{\gamma}^\alpha$, the plastic flow equation is further generalised

$$\bar{\boldsymbol{L}}^p = \dot{\boldsymbol{F}}^p\boldsymbol{F}^{p\,-1}, \quad \bar{\boldsymbol{L}}^p = \sum_{\alpha=1}^{n_\mathrm{syst}} \dot{\gamma}^\alpha \bar{\boldsymbol{s}}^\alpha \otimes \bar{\boldsymbol{m}}^\alpha, \tag{5}$$

$\bar{\boldsymbol{s}}^\alpha$ being the slip direction vector and $\bar{\boldsymbol{m}}^\alpha$ being the slip plane normal vector of the α-th slip system $\{\bar{\boldsymbol{s}}^\alpha, \bar{\boldsymbol{m}}^\alpha\}$. The slip system vectors have the properties $\bar{\boldsymbol{s}} \cdot \bar{\boldsymbol{m}} = 0$ and

thus $(\bar{\boldsymbol{s}}^\alpha \otimes \bar{\boldsymbol{m}}^\alpha)(\bar{\boldsymbol{s}}^\alpha \otimes \bar{\boldsymbol{m}}^\alpha) = \boldsymbol{0}$. The generalisation in (5) leads to the modified evolution equation of the plastic deformation gradient depending on the plastic slips

$$\dot{\boldsymbol{F}}^p = \left[\sum_\alpha \dot{\gamma}^\alpha \, \bar{\boldsymbol{s}}^\alpha \otimes \bar{\boldsymbol{m}}^\alpha\right] \boldsymbol{F}^p. \tag{6}$$

2.2 The resolved Schmid stress

The SCHMID stress τ^α is the projection of $\bar{\boldsymbol{\Sigma}}$ onto the slip system $\bar{\boldsymbol{s}}^\alpha \otimes \bar{\boldsymbol{m}}^\alpha$

$$\tau^\alpha = (\mathrm{dev}[\bar{\boldsymbol{\Sigma}}] \cdot \bar{\boldsymbol{m}}^\alpha) \cdot \bar{\boldsymbol{s}}^\alpha = \mathrm{dev}[\bar{\boldsymbol{\Sigma}}] : \bar{\boldsymbol{s}}^\alpha \otimes \bar{\boldsymbol{m}}^\alpha. \tag{7}$$

As the slip system tensor $\bar{\boldsymbol{s}}^\alpha \otimes \bar{\boldsymbol{m}}^\alpha$ is purely deviatoric, only the deviator of the stress tensor contributes to the resolved stress. With the relations in (4) and some straightforward recast, it is

$$\tau^\alpha = \boldsymbol{R}^{e\,T} \boldsymbol{\tau} \boldsymbol{R}^e : \bar{\boldsymbol{s}}^\alpha \otimes \bar{\boldsymbol{m}}^\alpha. \tag{8}$$

2.3 Elastic response

The elastic part of the deformation is gained from a NEO-HOOKEean strain energy function. Due to assumed isotropy within the elastic contribution, the description is given in terms of the elastic left CAUCHY-GREEN tensor $\boldsymbol{b}^e$. Applying a volumetric-deviatoric split yields

$$\rho\psi(\boldsymbol{b}^e_{\mathrm{iso}},\, \mathrm{J}^e) = \frac{\mu}{2}\,(\mathrm{tr}\,\boldsymbol{b}^e_{\mathrm{iso}} - 3) + \frac{\kappa}{2}\,(\ln \mathrm{J}^e)^2 \tag{9}$$

$$\boldsymbol{\tau} = 2\,\rho\,\frac{\partial \psi}{\partial \boldsymbol{b}^e}\,\boldsymbol{b}^e = \mu\,\mathrm{dev}(\boldsymbol{b}^e_{\mathrm{iso}}) + \kappa\,\ln \mathrm{J}^e\,\boldsymbol{1}, \quad \mathrm{dev}(\boldsymbol{\tau}) = \mu\,\mathrm{dev}(\boldsymbol{b}^e_{\mathrm{iso}}),\ \mathrm{vol}(\boldsymbol{\tau}) = \kappa\,\ln \mathrm{J}^e\,\boldsymbol{1}. \tag{10}$$

Because slip-system tensors are deviatoric by construction, their internal product by the hydrostatic KIRCHHOFF stress components vanishes and the SCHMID stress in (8) remains

$$\tau^\alpha = \mu\,\bar{\boldsymbol{s}}^\alpha_{\mathrm{iso}} \cdot \bar{\boldsymbol{m}}^\alpha_{\mathrm{iso}}, \quad \bar{\boldsymbol{s}}^\alpha_{\mathrm{iso}} = \boldsymbol{F}^e_{\mathrm{iso}} \cdot \bar{\boldsymbol{s}}^\alpha, \quad \bar{\boldsymbol{m}}^\alpha_{\mathrm{iso}} = \boldsymbol{F}^e_{\mathrm{iso}} \cdot \bar{\boldsymbol{m}}^\alpha. \tag{11}$$

2.4 A rate-dependent formulation via a viscoplastic power-law

A rate-dependent theory enables the modeling of creep in single crystals and is performed by the introduction of a power law-type constitutive equation for the rates $\dot{\gamma}^\alpha$ of inelastic deformation in the slip systems

$$\dot{\gamma}^\alpha = \dot{\gamma}_0\,\frac{\tau^\alpha}{\tau_y}\left(\frac{|\tau^\alpha|}{\tau_y}\right)^{m-1} = \dot{\gamma}_0\,\tau^\alpha\,|\tau^\alpha|^{m-1}\,\tau_y^{-m}, \tag{12}$$

$\dot{\gamma}_0$ and τ_y being the reference shear rate and slip resistance, and m being a rate-sensivity parameter. Within an isotropic TAYLOR hardening model, the evolution for the slip resistance τ_y is considered

$$\dot{\tau}_y = \sum_\alpha H \cdot |\dot{\gamma}^\alpha|, \quad \gamma = \int_0^t \dot{\gamma}\,dt, \quad \dot{\gamma} = \sum_\alpha \dot{\gamma}^\alpha. \tag{13}$$

3 INCREMENTAL KINEMATICS

The slip rate is discretised with a standard backward EULER integration in order to obtain incremental evolution equations for the update of the evolving quantities

$$\Delta\gamma^\alpha = \Delta t\, \dot{\gamma}^\alpha\,(\boldsymbol{F}^e)\,. \tag{14}$$

The implicit exponential integrator is then used to discretise the plastic flow equation (6)

$$\boldsymbol{F}^p_{n+1} = \exp\left[\sum_\alpha \Delta\gamma^\alpha \bar{\boldsymbol{s}}^\alpha \otimes \bar{\boldsymbol{m}}^\alpha\right] \cdot \boldsymbol{F}^p_n. \tag{15}$$

Due to the property $\det[\exp(\bar{\boldsymbol{s}}^\alpha \otimes \bar{\boldsymbol{m}}^\alpha)] = \exp[\mathrm{tr}\,(\bar{\boldsymbol{s}}^\alpha \otimes \bar{\boldsymbol{m}}^\alpha)] = \exp(0) = 1$, it preserves the plastic volume. Here, $\boldsymbol{F}^{e\,\mathrm{trial}}_{n+1} = \boldsymbol{f}_{n+1}\,\boldsymbol{F}^e_n$, is the *trial* elastic deformation gradient with $\boldsymbol{f}_{n+1} = \boldsymbol{F}_{n+1}\,\boldsymbol{F}^{-1}_n = \boldsymbol{1} + \mathrm{grad}_n\,(\Delta\boldsymbol{u})$ and $\mathrm{J}_{n+1} = \det\boldsymbol{F}_{n+1}$, $\boldsymbol{F}^{e\,\mathrm{trial}}_{\mathrm{iso}} = \mathrm{J}^{-1/3}_{n+1}\,\boldsymbol{F}^{e\,\mathrm{trial}}_{n+1}$, so that an exponential update for the new elastic deformation gradient can be obtained

$$\boldsymbol{F}^e_{n+1} = \boldsymbol{F}^{e\,\mathrm{trial}}_{n+1} \cdot \exp\left[\sum_\alpha -\Delta\gamma^\alpha \bar{\boldsymbol{s}}^\alpha \otimes \bar{\boldsymbol{m}}^\alpha\right]. \tag{16}$$

The current *trial* resolved shear stress $\tau^{\alpha\,\mathrm{trial}}_{n+1}$, cf. (11), is obtained with the current orientation of the crystal through rotation of the slip system with the trial elastic deformation gradient

$$\tau^{\alpha\,\mathrm{trial}}_{n+1} = \mu\,\bar{\boldsymbol{s}}^{\alpha\,\mathrm{trial}}_{\mathrm{iso}} \cdot \bar{\boldsymbol{m}}^{\alpha\,\mathrm{trial}}_{\mathrm{iso}}, \quad \bar{\boldsymbol{s}}^{\alpha\,\mathrm{trial}}_{\mathrm{iso}} = \boldsymbol{F}^{e\,\mathrm{trial}}_{\mathrm{iso}} \cdot \bar{\boldsymbol{s}}^\alpha, \quad \bar{\boldsymbol{m}}^{\alpha\,\mathrm{trial}}_{\mathrm{iso}} = \boldsymbol{F}^{e\,\mathrm{trial}}_{\mathrm{iso}} \cdot \bar{\boldsymbol{m}}^\alpha. \tag{17}$$

3.1 Equilibrating the plastic state

Omitting the subscript $n+1$, a residual based on the exponential map is defined to equilibrate the plastic state, leading to a local NEWTON-RAPHSON algorithm through a TAYLOR expansion about the reached point $\boldsymbol{F}^e_k$

$$\boldsymbol{R}(\boldsymbol{F}^e) := \boldsymbol{F}^e - \boldsymbol{F}^{e\,\mathrm{trial}} \cdot \exp\left[\sum_\alpha -\Delta\gamma^\alpha \bar{\boldsymbol{s}}^\alpha \otimes \bar{\boldsymbol{m}}^\alpha\right] = \boldsymbol{0}, \tag{18}$$

and

$$\boldsymbol{R}_k + \partial_{\boldsymbol{F}^e_k}\boldsymbol{R}(\boldsymbol{F}^e_k) : \Delta\boldsymbol{F}^e_k = \boldsymbol{0}, \tag{19}$$

$$\Delta\boldsymbol{F}^e_k = -\left[\partial_{\boldsymbol{F}^e_k}\boldsymbol{R}(\boldsymbol{F}^e_k)\right]^{-1} : \boldsymbol{R}_k, \quad \boldsymbol{F}^e_{k+1} = \boldsymbol{F}^e_k + \Delta\boldsymbol{F}^e_k, \tag{20}$$

with the important derivatives

$$\left[\partial_{\boldsymbol{F}^e}\boldsymbol{R}(\boldsymbol{F}^e)\right]_{ijkl} = \delta_{ik}\delta_{jl} + F^{e\,\mathrm{trial}}_{im}\,\mathbb{E}_{mjpq}\left[\sum_\alpha \bar{\boldsymbol{s}}^\alpha \otimes \bar{\boldsymbol{m}}^\alpha \otimes \partial_{\boldsymbol{F}^e}\Delta\gamma^\alpha\right]_{pqkl} \tag{21}$$

$$\mathbb{E}_{mjpq} = \frac{\partial \exp\left(\left[-\sum_\alpha \Delta\gamma^\alpha(\boldsymbol{F}^e)\,\bar{\boldsymbol{s}}^\alpha \otimes \bar{\boldsymbol{m}}^\alpha\right]_{mj}\right)}{\partial\left[-\sum_\alpha \Delta\gamma^\alpha(\boldsymbol{F}^e)\,\bar{\boldsymbol{s}}^\alpha \otimes \bar{\boldsymbol{m}}^\alpha\right]_{pq}}, \tag{22}$$

and

$$\partial_{\boldsymbol{F}^e} \Delta\gamma^\beta = \Delta t\, \dot\gamma_0\; m\; |\tau^\alpha|^{m-1}\; \tau_y^{-m}\; \left[\Xi^{\alpha\,\beta}\right]^{-1}\; \partial_{\boldsymbol{F}^e}\, \tau^\alpha \tag{23}$$

$$\partial_{\boldsymbol{F}^e}\, \tau^\alpha = -\frac{2}{3}\, \tau^\alpha\, \boldsymbol{F}^{e\,-T} + \mu\, \mathrm{J}^{-1/3}\, [\bar{\boldsymbol{m}}^\alpha_{\mathrm{iso}} \otimes \bar{\boldsymbol{s}}^\alpha + \bar{\boldsymbol{s}}^\alpha_{\mathrm{iso}} \otimes \bar{\boldsymbol{m}}^\alpha] \tag{24}$$

$$\Xi^{\alpha\,\beta} = \delta^{\alpha\,\beta} + \Delta t\, \dot\gamma_0\, m\, \tau^\alpha\; |\tau^\alpha|^{m-1}\, \tau_y^{-m-1} \sum\nolimits_\beta H\, \mathrm{sign}(\Delta\gamma^\beta). \tag{25}$$

4 MODEL OF THE POLYCRYSTAL

4.1 Voronoi cell grains

The polycrystal is modelled with three-dimensional VORONOI cell shaped grains. Through the DELAUNAY triangulation of a given random point seed, a polycrystal of arbitrary size can be obtained through stating the size of the bounding box.

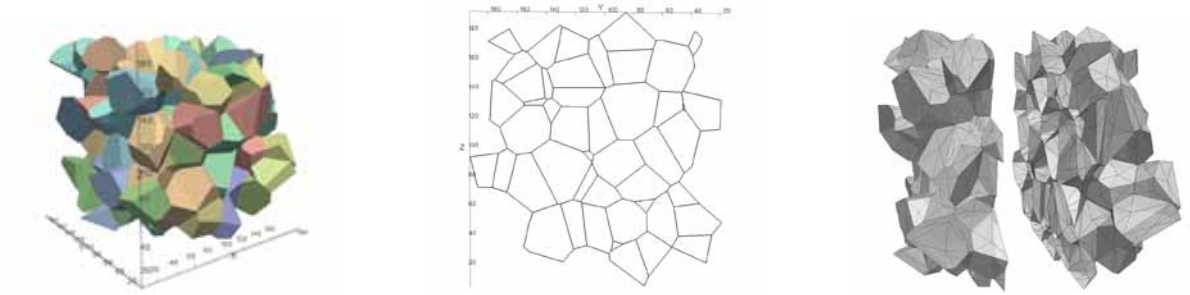

(a) Polycrystal consisting of VORONOI cell grains.

(b) Cut through polcrystalline structure.

(c) Three-dimensional view into the cutted polycrystal.

Figure 2: Polycrystalline model within bounding box $200 \times 200 \times 200\,\mu$m. The VORONOI cell shaped crystal grains are obtained through DELAUNAY triangulation of a random point seed.

4.2 Euler angle rotation of the grains

In order to realise randomly orientated slip systems in each grain of the undeformed polycrystalline structure, the slip system vectors are rotated around the cartesian axes about three EULER angles Φ, Θ and Ψ according to a y-convention, see Fig. 3; Performed is a rotation about the z-axis, the y-axis and the new z-axis, successively,

$$\boldsymbol{R}_\Psi = \begin{bmatrix} \cos\Psi & -\sin\Psi & 0 \\ \sin\Psi & \cos\Psi & 0 \\ 0 & 0 & 1 \end{bmatrix} \quad \boldsymbol{R}_\Theta = \begin{bmatrix} \cos\Theta & 0 & \sin\Theta \\ 0 & 1 & 0 \\ -\sin\Theta & 0 & \cos\Theta \end{bmatrix} \quad \boldsymbol{R}_\Phi = \begin{bmatrix} \cos\Phi & -\sin\Phi & 0 \\ \sin\Phi & \cos\Phi & 0 \\ 0 & 0 & 1 \end{bmatrix}, \tag{26}$$

$$\boldsymbol{R} = \boldsymbol{R}_\Psi \cdot \boldsymbol{R}_\Theta \cdot \boldsymbol{R}_\Phi. \tag{27}$$

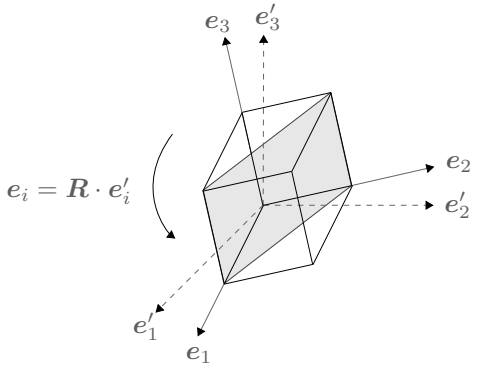

Figure 3: Rotation of the axes around random EULER angles

5 NUMERICAL HOMOGENISATION

5.1 Boundary conditions

Based on the construction of polycrystalline structures according to Sec. 4, polycrystals of several sizes are modelled, representing the microstructure of the polycrystalline material, see Fig. 2. The displacement field $\boldsymbol{u}$ is given through a constant displacement gradient $\boldsymbol{H}$ on the entire boundary of the polycrystal

$$\boldsymbol{u}|_{\mathrm{d}\Omega} = \boldsymbol{H} \cdot \boldsymbol{X}|_{\mathrm{d}\Omega}\,, \quad \boldsymbol{H} = \text{const.} \tag{28}$$

5.2 Volume average

In order to approach the prediction of an overall material behaviour of the representative volume element and hence of the macroscopic material, the volume averages of the deformation gradient $\boldsymbol{F}$ and the 1st PIOLA-KIRCHHOFF stress tensor $\boldsymbol{P}$ over the volume $V = \int_\Omega \mathrm{d}\Omega$ are defined as

$$\langle \boldsymbol{F} \rangle_\Omega := \frac{1}{V} \int_\Omega \boldsymbol{F} \; \mathrm{d}\Omega \tag{29}$$

$$\langle \boldsymbol{P} \rangle_\Omega := \frac{1}{V} \int_\Omega \boldsymbol{P} \; \mathrm{d}\Omega. \tag{30}$$

5.3 Overall polycrystalline behaviour

Differently sized polycrystals, from a size edge range between 100 and 200 μm, see Fig. 4, are subjected to pure shear loading through the displacement gradient $\boldsymbol{H} = \boldsymbol{e}_1 \otimes \boldsymbol{e}_2$. The number of crystal grains depend on the size and are shown in Tab. 1. The material parameters for all the microstructures are equal; it is the bulk modulus $\kappa = 152.2$ GPa, the shear modulus $\mu = 79.3$ GPa, and the parameters for the viscoplastic range amount to $H = 1.0$ GPa, $\tau_{y0} = 180$ MPa, $\dot{\gamma}_0 = 0.0005$ and $m = 3.0$. In order to obtain a statistically admissible response, 200 tests are computed for each size with body-centered cubic crystals with 24 slip system vectors of Tab. 2.

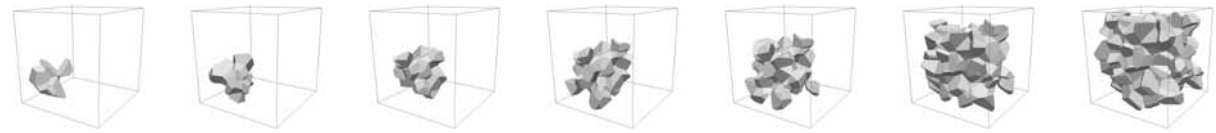

(a) 100 μm (b) 110 μm (c) 130 μm (d) 140 μm (e) 150 μm (f) 180 μm (g) 200 μm

Figure 4: Polycrystals of different sizes. The shown cube represents a bounding box of size $200 \times 200 \times 200$ μm.

Table 1: Number of grains for polycrystal edge sizes

bounding box size edge [μm]	100	110	130	140	150	180	200
number of grains	6	13	20	32	45	107	157

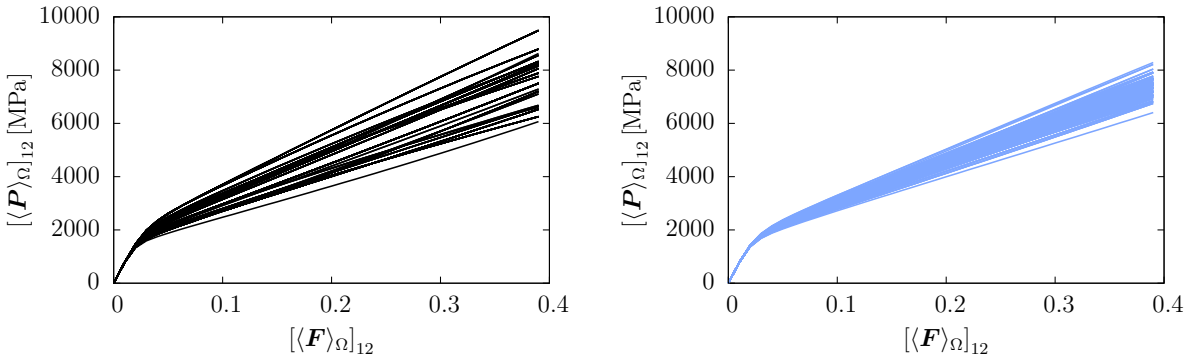

(a) Polycrystal within the bounding box $100 \times 100 \times 100$ μm.

(b) Polycrystal within the bounding box $150 \times 150 \times 150$ μm.

Figure 5: Stress-strain relations of the polycrystals of different sizes.

Table 2: 24 slip system vectors for body-centered cubic crystals

$\bar{\boldsymbol{s}}^\alpha$	$\bar{\boldsymbol{m}}^\alpha$	$\bar{\boldsymbol{s}}^\alpha$	$\bar{\boldsymbol{m}}^\alpha$	$\bar{\boldsymbol{s}}^\alpha$	$\bar{\boldsymbol{m}}^\alpha$	$\bar{\boldsymbol{s}}^\alpha$	$\bar{\boldsymbol{m}}^\alpha$
$[\bar{1}11]$	$(0\bar{1}1)$	$[111]$	$(0\bar{1}1)$	$[11\bar{1}]$	(011)	$[1\bar{1}1]$	(011)
$[\bar{1}11]$	(101)	$[111]$	$(\bar{1}01)$	$[11\bar{1}]$	(101)	$[1\bar{1}1]$	$(\bar{1}01)$
$[\bar{1}11]$	(110)	$[111]$	$(\bar{1}10)$	$[11\bar{1}]$	$(\bar{1}10)$	$[1\bar{1}1]$	(110)
$[\bar{1}11]$	(211)	$[111]$	$(\bar{2}11)$	$[11\bar{1}]$	$(2\bar{1}1)$	$[1\bar{1}1]$	$(21\bar{1})$
$[\bar{1}11]$	$(12\bar{1})$	$[111]$	$(1\bar{2}1)$	$[11\bar{1}]$	$(\bar{1}21)$	$[1\bar{1}1]$	(121)
$[\bar{1}11]$	$(1\bar{1}2)$	$[111]$	$(11\bar{2})$	$[11\bar{1}]$	(112)	$[1\bar{1}1]$	$(\bar{1}12)$

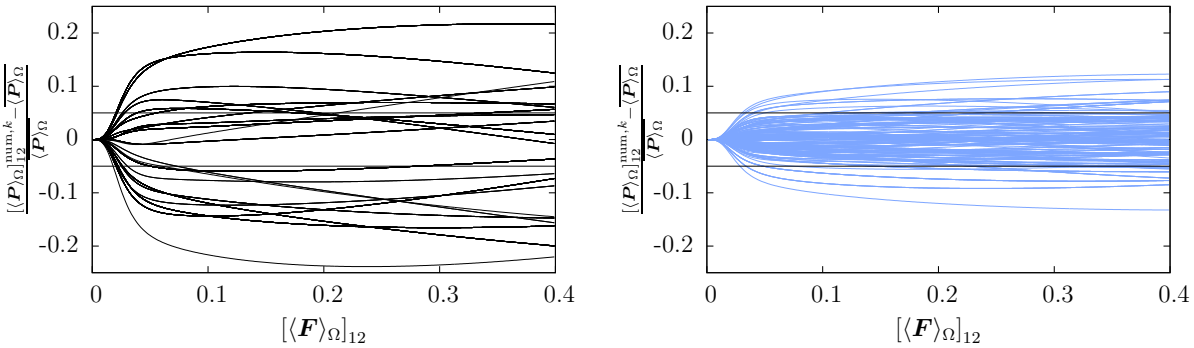

(a) Polycrystal within the bounding box $100 \times 100 \times 100$ μm.

(b) Polycrystal within the bounding box $150 \times 150 \times 150$ μm.

Figure 6: Relative errors with respect to mean value of the computations.

As an example, the overall stress-strain relations for 200 polycrystalline structures of edge size 100 and 150 μm, respectively, are shown in Fig. 5. Whereas the response of the smaller polycrystal shows a rather scattering stress-strain behaviour due to the remaining high influence of the boundary loading, the larger polycrystal presents a more representative behaviour of the microstructure. Expressed this in terms of the relative error in the homogenised 1$^{\text{st}}$ PIOLA-KIRCHHOFF stresses $\langle \boldsymbol{P} \rangle_\Omega$, the error reaches a level of 20 % and more over the whole deformation, see Fig. 6. Increasing the size of the polycrystal results in a decrease of the relative error. In order to restrict the error to 5 %, error lines at ± 5 % are included.
The same effect applies for the normalised standard deviation $\sigma(\langle P_{ij} \rangle_\Omega) / \overline{||\langle P_{ij} \rangle_\Omega||}$ with

$$\sigma(\langle P_{ij} \rangle_\Omega) = \sqrt{\frac{1}{n} \sum_{k=1}^{n} \left(\langle P_{ij} \rangle_\Omega^k - \overline{\langle P_{ij} \rangle_\Omega} \right)^2} \tag{31}$$

$$\overline{\langle P_{ij} \rangle_\Omega} = \frac{1}{n} \sum_{k=1}^{n} \langle P_{ij} \rangle_\Omega^k \tag{32}$$

$$\overline{||\langle P_{ij} \rangle_\Omega||} = \frac{1}{n} \sum_{k=1}^{n} \left|| \langle P_{ij} \rangle_\Omega^k \right|| \tag{33}$$

Fig. 7(a) shows the normalised standard deviation of the component $[\langle \boldsymbol{P} \rangle_\Omega]_{12}$ for different polycrystals over the deformation, Fig. 7(b) represents it over the polycrystal size in terms of the crystal grain quantity. From a grain number of about 20 on, the standard deviation does not decrease significantly anymore, whereas the ± 5 % error measure requires polycrystalline structures of 100 grains and more.

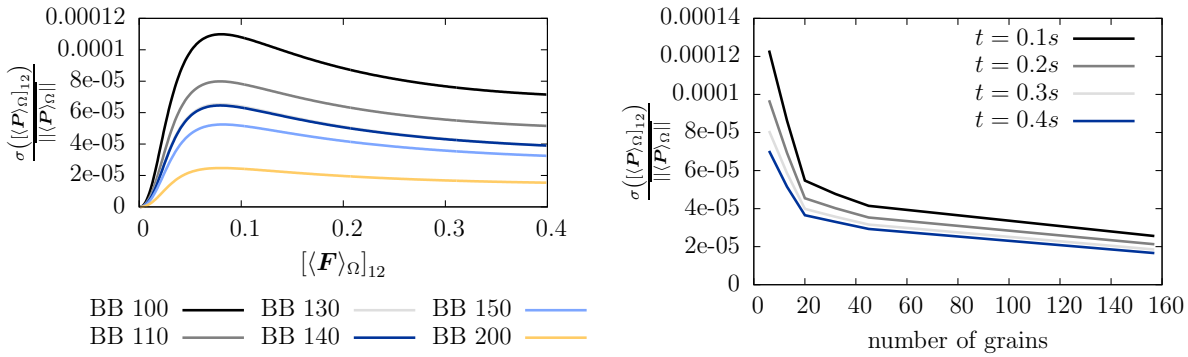

(a) Standard deviation over time.

(b) Standard deviation over grain number.

Figure 7: Normalised standard deviation of the polycrystals of different sizes for a population of 200 computations.

6 CONCLUDING REMARKS AND OUTLOOK

6.1 Effective material properties

Assuming that the stresses from the volume averaging procedure are the same as from an effective material assumption

$$\langle \boldsymbol{P} \rangle_\Omega = \boldsymbol{P}^{\text{eff}} = \boldsymbol{P}(\langle \boldsymbol{F} \rangle_\Omega) = \boldsymbol{P}(\boldsymbol{F}^{\text{eff}}), \tag{34}$$

the determination of the effective material parameters can be performed based on a least square fit between the mean stresses out of n performed computations and the stresses from an effective constitutive assumption

$$\Pi := \left[\frac{1}{n} \sum_{k=1}^{n} \left(\langle \boldsymbol{P} \rangle_\Omega^k \right) - \boldsymbol{P}(\boldsymbol{F}^{\text{eff}}(\boldsymbol{\kappa}^{\text{eff}})) \right]^2 \rightarrow \text{minimum} \tag{35}$$

$$\boldsymbol{\kappa}^{\text{eff}} := \left[\boldsymbol{\kappa}_{el}^{\text{eff}}, \boldsymbol{\kappa}_{pl}^{\text{eff}} \right]^T . \tag{36}$$

Due to the volumetric-deviatoric split of the constitution, see (10), both parts of the deformation can be separated and reveals quite an easy way to determine first the isotropic elastic material parameters $\boldsymbol{\kappa}_{el}^{\text{eff}}$ by remaining in the elastic range of the deformation. Having determined the parameters with (35), also for varying elastic parameters within the crystal grains, the assignment of the plastic parameters $\boldsymbol{\kappa}_{pl}^{\text{eff}}$ can be done. Eventually, the gained effective material model representing the microstructural behaviour has to be validated for different kinds of boundary conditions and constraints of real forming processes.

7 ACKNOWLEDGEMENTS

Financial support for this research was provided by the Deutsche Forschungsgemeinschaft (DFG) under grant SFB TR 73. This is gratefully acknowledged.

REFERENCES

[1] Anand, L. Single-crystal elasto-viscoplasticity: application to texture evolution in polycrystalline metals at large strains. *Comput. Meth. Appl. Mech. Eng.* (2004) **193**:5359–5383.

[2] Asaro, R.J. Crystal plasticity. *J. Appl. Mech.* (1983) **50**:921–934.

[3] Cuitiño, A.M. and Ortiz, M. Computational modelling of single crystals. *Modelling Simul. Mater. Sci. Eng.* (1992) **1**:225–263.

[4] De Souza, E.A. The exact derivative of the exponential of an unsymmetric tensor. *Comput. Meth. Appl. Mech. Eng.* (2001) **190**:2377–2383.

[5] De Souza, E.A. and Perić, D. and Owen, D.R.J. *Computational methods for plasticity. Theory and applications*. John Wiley and Sons Ltd Publication, (2008).

[6] Hosford, W.F. *The mechanics of crystals and textured polycrystals*. Oxford Engineering Science Series (1993).

[7] Itskov, M. Computation of the exponential and other isotropic tensor functions and their derivatives. *Comput. Meth. Appl. Mech. Eng.* (2003) **192**:3985–3999.

[8] Mandel, J. *Plasticité classique et viscoplasticité*. CISM Lecture Notes No. 97, International center for mechanical sciences, Springer Verlag, New York (1972).

[9] Miehe, C. Exponential map algorithm for stress updates in anisotropic multiplicative elastoplasticity for single crystals. *Int. J. Numer. Methods Eng.* (1996) **50**:273–298.

[10] Needleman, A. and Asaro, R.J. and Lemonds, J. and Peirce, D. Finite element analysis of crystalline solids. *Comput. Meth. Appl. Mech. Eng.* (1985) **52**:689–708.

[11] Steinmann, P. and Stein, E. On the numerical treatment and analysis of finite deformation ductile single crystal plasticity. *Comput. Meth. Appl. Mech. Eng.* (1996) **129**:235–254.